Corrosion Science 200 (2022) 110202

Contents lists available at ScienceDirect

Corrosion Science

journal homepage: www.elsevier.com/locate/corsci

Corrosion characteristics of Mo and TZM alloy for plasma facing components in molten lithium at 623 K

X.C. Meng [a,b], L. Li [b], C.L. Li [b], D. Andruczyk [c], K. Tritz [d], R. Maingi [e], M. Huang [b], D.H. Zhang [b], W. Xu [a,b], Z. Sun [b,e], G.Z. Zuo [b,*], J.S. Hu [b,f,**]

[a] Institute of Energy, Hefei Comprehensive National Science Center, Hefei 230031, China
[b] Institute of Plasma Physics, Chinese Academy of Sciences, Hefei 230031, China
[c] Center for Plasma Material Interactions, Department of Nuclear, Plasma and Radiological Engineering, University of Illinois Urbana-Champaign, Urbana, IL 61801, USA
[d] Johns Hopkins University, Baltimore, MD 21211, USA
[e] Plasma Physics Laboratory, Princeton University, Princeton, NJ 08543, USA
[f] CAS key Laboratory of Photovoltaic and energy conservation materials, Hefei 230031, China

ARTICLE INFO

Keywords:
Corrosion
Liquid lithium
Mo-based alloy
PFM
Blanket components

ABSTRACT

In this study, the corrosion behaviours of molybdenum (Mo) and a Mo-based alloy (TZM) were investigated using a static immersion corrosion technique. Weight loss, surface microstructure, and corrosion depth of Mo and the TZM alloy were correlated with elements. The compatibility of Mo and the TZM alloy in static liquid Li was suitable. Mo demonstrated uniform corrosion with a homogenous dissolution of free C and Mo, and TZM alloy exhibited a nonuniform corrosion behaviour with a preferential grain boundary attack caused by the selective dissolution of free C, Ti, and Zr. When the surface oxidation layer of the samples was consumed, free C from Mo and TZM diffused into molten Li to form Li_2C_2 and then was captured by Zr, Ti, and Mo to form thermodynamically stable carbides, which resulted in the enrichment of the C layer near the sample surfaces. In addition, Ti and Zr acted as N-trappers in liquid Li; the formation of Zr and Ti nitrides resulted in the enrichment of N, Ti, and Zr elements on the surface and led to TZM corrosion increase. Thus, Zr and Ti depletion, pitting, and grain boundary corrosion were problematic for TZM under long-term exposure to liquid Li. Reducing the content of free C and nonmetallic N and increasing the amount of Ti and Zr carbides on the surface of and inside the raw TZM alloy helped improve the corrosion resistance of TZM in liquid Li.

1. Introduction

The liquid metal blanket concept is promising for realising a high-power-density DEMO fusion blanket system due to its advantages such as continuous replacement of breeders for reprocessing, no radiation damage of the breeder, simpler blanket structure, and better thermal transfer than solid blanket concepts [1,2]. Two liquid metals of pure Li and eutectic lead lithium alloy (Pb–Li) are considered promising candidates to meet fusion reactor specifications. Liquid Li blankets have several inherent advantages, including a high tritium breeding ratio without the equipment of an additional neutron multiplier and high tritium recovery efficiency even under a low content of approximately 1 ppm, over eutectic Pb–Li; moreover, the system pressure of tritium is $< 10^{-6}$ Pa, which is six orders of magnitude less than that of the Pb–Li system [3,4]. Furthermore, the interaction of plasma with the first wall is a main problem in achieving high-power and long-pulse plasma in fusion devices [5]. Selection of appropriate plasma facing materials (PFMs) and the wall conditioning technique are two important aspects [6–8] to obtain high-performance plasma. Liquid Li, serving as PFM, has large potential to improve plasma performance. Various static liquid Li walls, including free surface and capillary pore structures, have been investigated in many fusion devices, and encouraging results have been obtained; for example, plasmas with low recycling, reduced impurity levels, and high confinement have been achieved. In addition, flowing liquid Li walls can withstand high heat loads and particle fluxes of plasma to prevent the blistering, cracking, and melting of underlying

* Corresponding author.
** Corresponding author at: Institute of Plasma Physics, Chinese Academy of Sciences, Hefei 230031, China.
E-mail addresses: zuoguizh@ipp.ac.cn (G.Z. Zuo), hujs@ipp.ac.cn (J.S. Hu).

https://doi.org/10.1016/j.corsci.2022.110202
Received 27 July 2021; Received in revised form 17 February 2022; Accepted 21 February 2022
Available online 4 March 2022
0010-938X/

Table 1
The chemical compositions and ratios of materials.

Li	Composition	**Na**	**K**	**Ca**	**Fe**	**N**	**Si**	**Cl**	**Al**	**Ni**	**Cu**
	wt%	0.0045	0.0002	0.0015	0.003	0.0027	0.002	0.002	0.001	0.002	0.001
Mo	Composition	**Al**	**Ca**	**Fe**	**C**	**Mg**	**Si**	**Ni**	**N**	**O**	**Mo**
	wt%	0.005	0.004	0.015	0.02	0.005	0.010	0.005	0.003	0.010	Bal
TZM	Composition	**Ti**	**Zr**	**C**	**Fe**	**Ni**	**Si**	**N**	**O**	**Mo**	/
	wt%	0.50	0.09	0.02	0.010	0.005	0.010	0.002	0.030	Bal	/

solid substrates during plasma discharge [9–14]. Hence, liquid Li is now being considered a potential candidate for plasma-facing components in the first wall as a limiter/divertor in fusion devices.

Mo and Mo-based alloys are suitable materials for high-temperature structural applications due to their excellent mechanical properties of high tensile strength and substantially high creep strength at high temperatures [15]. In both a fusion reactor and an advanced nuclear power plant, structural materials are highly desired for increasing the thermal efficiency and securing system safety during a long-term service at high temperatures. Mo- and Nb-based alloys are promising materials for structural applications in advanced nuclear plants [16]. Moreover, Mo exhibits properties, such as high thermal conductivity, low hydrogen isotope retention, and low sputtering rate, which are suitable for the wall components of fusion devices. In 2012, EAST substituted graphite tiles with Mo tiles to facilitate metal wall operations [7]. For the JT-60 device, the first stage of PFMs is TiC/Mo [17]. In addition, Mo has better wettability with liquid Li than other candidate materials, such as tungsten and stainless steel [18,19]. Therefore, to improve the spread area of Li and corrosion resistance of wall components, Mo and Mo-based alloys have been used as substrate materials for a liquid Li limiter and a divertor in many fusion devices, such as NSTX [9], EAST, CDU-X [11], and FTU [20]. Mo and Mo-based alloys have played and will continue to play an important role in the nuclear field. For the Mo alloy materials utilised in the severe environment of the liquid alkali first wall, liquid blanket, and alkali metal-cooled fast breeder reactor, suitable compatibility with the liquid alkali metal is the first requirement. Liquid Li is an alkali metal with a high chemical reactivity and strong corrosion. Hence, corrosion resistance against Li is one of the most important properties and of general interest for use in such applications.

However, limited information regarding the compatibility of Mo-based alloys and liquid Li is available. Saito et al. [16] studied the corrosion behaviour of both binary Nb- and Mo-based alloys in liquid Li at 1473 K and showed that there were no cracks and few corrosion products on the surface of Mo-based alloys, and the weight change of binary Mo-based alloys was approximately 10 factors smaller than that of binary Nb-based alloys. Inoue et al. [21] also reported that Mo-based alloys exhibited higher corrosion resistance than Nb-based alloys in liquid Li, Mo–Re-based alloys showed mass gain due to corrosion, and the amount of mass gain increased with the corrosion time [15]. Katsuta et al. [22] reported that TZM and pure Mo showed mass gain when they were maintained at 873 K for 1018 h in liquid Li containing 0.1 mass% N, and the corrosion rates of Mo and TZM were 2 and 5 mm/yr, respectively. He et al. [23] investigated the effects of high-flux helium plasma irradiation on the corrosion behaviours of liquid Li on Mo surfaces. They found that after immersion in liquid Li, Mo showed slight corrosion regardless of exposure to plasma or not, and the diffusion of carbon to bulk was suppressed with a fuzz layer. These studies are important to understand the corrosion behaviours of Mo and Mo-based materials in liquid Li; however, they are not sufficient to understand the corrosion mechanism and evaluate the service life of these materials in liquid Li.

In consideration of the lifetime of Mo and Mo-based alloy parts and the safety of fusion devices with the use of liquid Li, the corrosion characteristics of Mo and Mo-based alloys in liquid Li must be well understood. Mo-based materials find several applications in the liquid Li first wall and blanket. The critical wetting temperature range of liquid Li on Mo and TZM surfaces is 558–603 K [18]. The higher is the temperature of the material substrate, the better is the wettability of the liquid Li. A suitable wettability is conducive to spread Li on the surface of the Mo alloy material. During plasma operations, the larger is the spread area of liquid Li on the limiter surface, the better is the performance of plasma [12]. In 2018, a new flowing liquid Li limiter with a TZM substrate, working at temperature range of 603–673 K, was developed during high-confinement plasmas in the EAST device [24]. In addition, the inlet and outlet temperature range of liquid Li is 603–883 K for liquid Li blanket concepts [25,26]. Thus, to further guide the design and application of Mo-based alloy components with liquid Li for the liquid Li first wall and blanket in fusion devices, the corrosion characteristics of Mo and Mo-based alloys in liquid Li must be studied at 603 or 883 K. The corrosion behaviour of Mo and TZM in liquid Li at 873 K was investigated [22]. Therefore, the corrosion characteristics of Mo-based alloys in liquid Li at low temperature must be studied. Considering the fluctuation of test temperatures, in this study, corrosion tests were conducted with Mo and the TZM alloy in liquid Li at 623 K. Then, the corrosion behaviours of Mo and TZM were compared. The corrosion mechanism regarding the transfer and chemical reaction of elements was studied. Finally, suggestions to restrain the corrosion of Mo-based alloys in molten Li were provided. The study results can provide valuable reference for the engineering design of candidate materials in the liquid-metal first wall and blanket system for future fusion reactors.

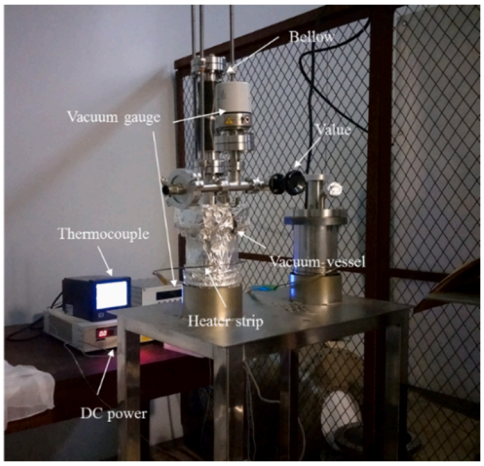

Fig. 1. Liquid metal testing device.

2. Experimental setup

2.1. Materials

The Mo and TZM samples were coupon-type with dimensions of 10 mm × 13 mm × 1 mm. Their surfaces were mechanically polished using diamond powders with particle diameters of 2.5 and 0.5 μm. Before the corrosion experiment, all the samples were cleaned ultrasonically with high-purity alcohol (99.9%). Metallic Li was supplied in ingots with a high purity of 99.9%. The chemical compositions of Mo, TZM, and Li are listed in Table 1. The mechanical properties of TZM considerably improved with the addition of 0.5% Ti and 0.09% Zr. To avoid mass transfer, the vessel and mounting points of the experimental device were

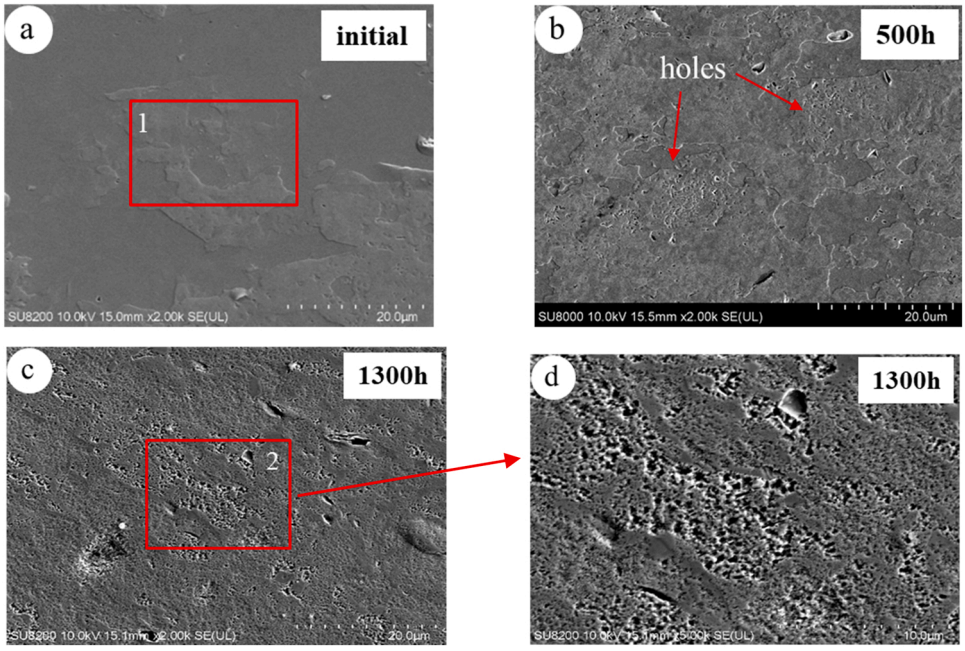

Fig. 2. Surface micrographs and EDS analysis area of Mo sample before and after being dipped in liquid Li: (a) before test, (b) after exposure to liquid Li for 500 h, (c) after exposure to liquid Li for 1300 h, and (d) higher magnification of the corrosion area of (c).

made of Mo. Eight samples and 137 g of Li were used in each experiment. The ratio of Li volume to the total surface area of the samples was approximately 10.28 cm.

2.2. Static corrosion test

Mo and TZM corrosion experiments were performed in a liquid metal testing device, which is considerably smaller than the previously employed device [27] (Fig. 1). The volume of the liquid metal testing device used was approximately 1.8 L. Before the experiment, to reduce the effect of gaseous impurities on the corrosion results, the device was heated to > 700 K by using a resistive heating element and pumped to a vacuum pressure of $< 10^{-4}$ Pa by utilising a turbo-molecular pump. Then, for each test, eight samples were attached to mounting points approximately 20 mm above the bottom of the test vessel. Approximately 137 g of Li was placed in a test vessel in the Ar atmosphere to prevent Li oxidation. Finally, the test vessel was heated to 623 K and kept at this temperature. The fluctuation of the temperature was within approximately 5 ℃. The depth of liquid Li was approximately 35 mm after Li completely melted, and the samples were completely immersed in liquid Li. After the experiments, the samples were removed from liquid Li by using a bellow. Then, residual Li on the sample surface was cleaned with high-purity alcohol.

2.3. Characterisation

The extent of corrosion was evaluated using the weight change and visual appearance of the samples. The weight change was determined using the weight loss method. An electronic balance with the accuracy of 0.01 mg was used to measure the sample weight. Each sample was weighed five times, and then, the average was used to evaluate the weight change. The weight loss rate V (in $g{\cdot}m^{-2}{\cdot}h^{-1}$) is defined as $V = (m_0–m_1)/St$, where m_0 and m_1 are the sample mass before and after immersion (g), respectively; S is the surface area of the sample (m^2); and t is the corrosion time (h). The corrosion depth rate was obtained using the equation $V_d = 8.76\ V/\rho$, where V is the weight loss rate, and ρ is the sample density (in g/cm^3).

Scanning electron microscope (SEM, Hitachi SU8200) with an energy dispersive spectrometry (EDS) and X-ray photoelectron spectroscopy (XPS, ESCALAB 250) as well as time-of-flight secondary ion mass spectrometry (TOF-SIMS) were used to characterise the microstructural and compositional changes of the corroded surface and cross-section. The cross-section of the sample was cut using a highly fine-focused ion beam (FIB). Vickers hardness was measured using a Vickers hardness testing machine under a load of 500 gf with a loading time of 15 s. Finally, the average of the results of five indentation tests was calculated.

3. Results and discussion

3.1. Weight loss

When exposed to liquid Li at 623 K for 1300 h, the weight loss rates of Mo and TZM were 0.5 and 1.0 g m^{-2}, respectively; these correspond to the weight loss rates of 4.0×10^{-4} and 7.8×10^{-4} g m^{-2} h^{-1}, respectively, which are equivalent to 0.34 and 0.67 μm a^{-1}, respectively, for the average corrosion depth rate assuming the densities of Mo and TZM to be 10.29 and 10.22 $g{\cdot}cm^{-3}$. The results demonstrate that the corrosion protection grade of Mo and TZM reaches 1. There are 10 grades of corrosion protection, from 1 to 10, where the smaller is the value, the stronger is the corrosion resistance of the material. As confirmed by Ref. [28], the weight loss rates of 304 and 316 L austenitic stainless steel (SS) are 2.3×10^{-3} and 6.4×10^{-4} $g{\cdot}m^{-2}$ h^{-1}, respectively, which are equivalent to 2.6 and 0.71 μm a^{-1} average corrosion depth rates under similar conditions of liquid Li at 600 K. The results show that the weight loss rates of Mo and TZM are lower than those of 304 and 316 L SS in liquid Li.

3.2. Morphology of corroded Mo and TZM

3.2.1. Microstructures of Mo samples after corrosion test

The microstructure and composition analyses of the specimens were performed using an SEM and EDS, respectively, before and after the corrosion experiment. The SEM micrographs of the Mo sample before and after corrosion are shown in Fig. 2. The corroded Mo sample shows the same metallic lustre as before the corrosion test after cleaning. The SEM image in Fig. 2(a) shows a flat and uniform Mo surface before the experiment. Fig. 2(b) and (c) show a uniform but hole-containing Mo

Table 2
Surface compositions of Mo samples before and after exposed to liquid Li.

Area	Surface composition (EDS result)	O	C	Mo
1	wt%	3.92	6.5	89.58
2	wt%	1.09	10.33	88.58

sample surface after exposure to liquid Li for 500 and 1300 h. After exposed to liquid Li for 1300 h, the Mo surface shows more holes than after exposure for 500 h. At a higher magnification, Fig. 2(d) shows holes with various sizes, and the largest hole diameter is approximately 2 μm. Moreover, no obvious corrosion particulate is observed on the surface of corroded Mo, which indicates that Mo demonstrates homogeneous corrosion, except for pitting in liquid Li.

The composition analysis areas of the Mo sample before and after the corrosion experiment are shown in Fig. 2(a) and (c), respectively. The composition change derived from the EDS analysis of the surface area is listed in Table 2. The depletion of Mo and O but enrichment of C is observed on the Mo surface after exposure to liquid Li.

To obtain the composition distribution from the surface of the corroded samples to the interior of the substrate, FIB and EDS line scan analyses were performed. Fig. 3(a) and (b) show the cross-section and

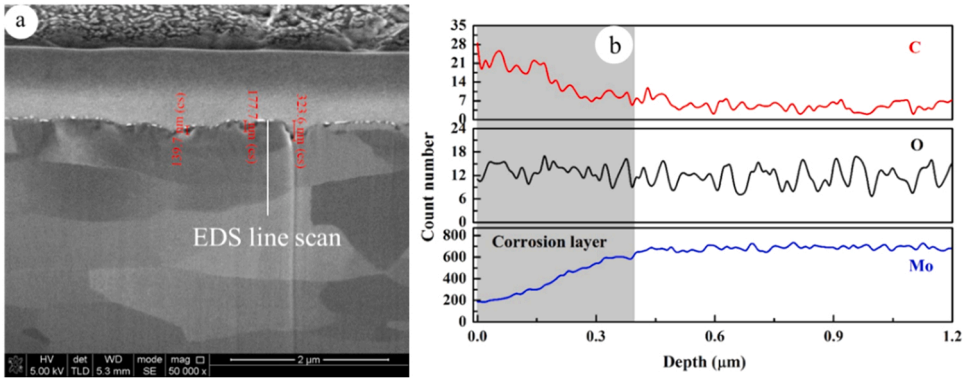

Fig. 3. SEM micrographs of the cross-section and EDS line scan results of Mo after exposure to Li for 1300 h.

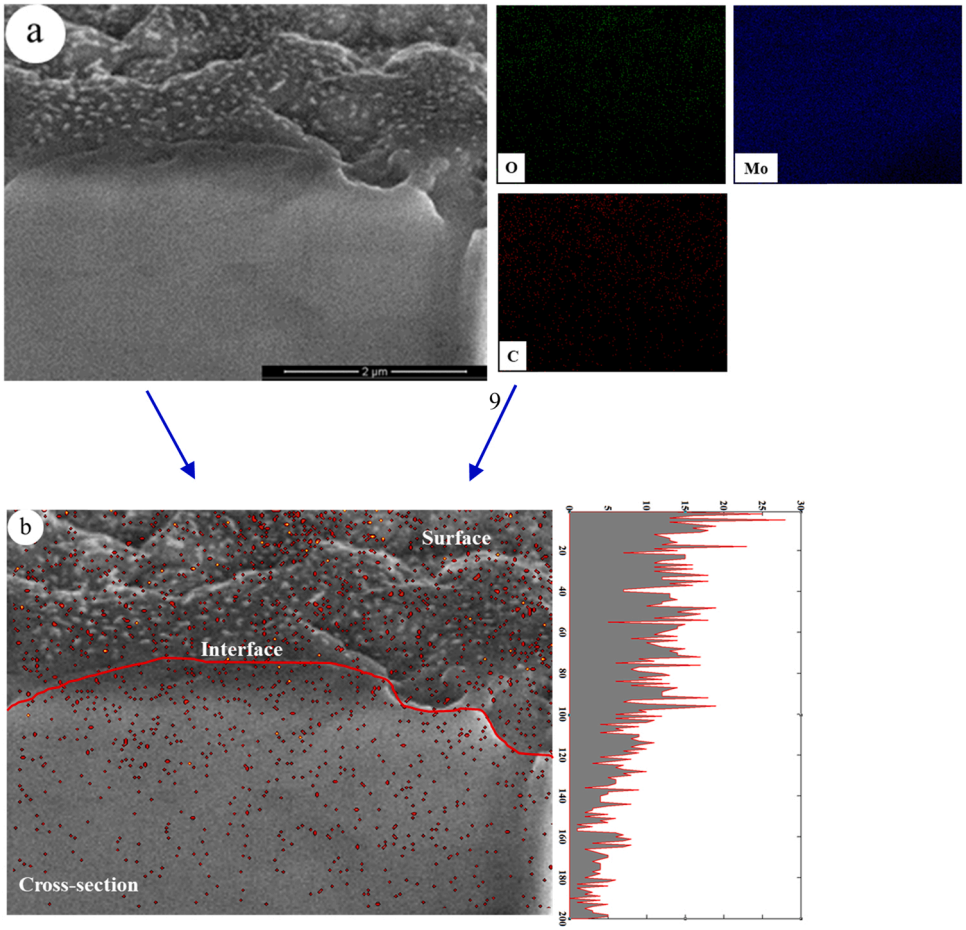

Fig. 4. SEM micrograph of the surface and cross-section of corroded Mo after exposure to liquid Li for 1300 h: (a) EDS elemental mapping analysis and (b) combinatorial diagram of C content and distribution.

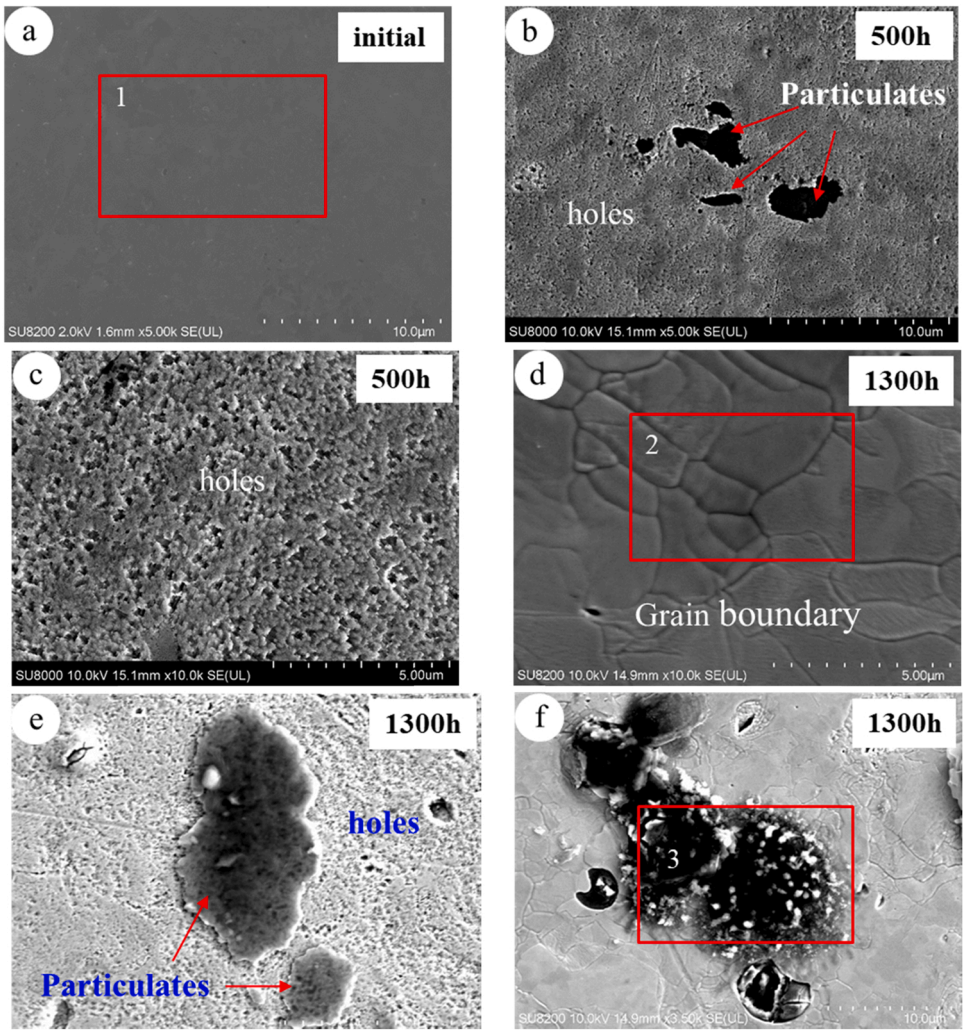

Fig. 5. Surface SEM micrographs and EDS analysis area of TZM before and after exposure to liquid Li for 500 and 1300 h: (a) before corrosion test, (b) after exposure for 500 h, (c) morphology of holes, (d) after exposure for 1300 h, grain boundary corrosion, (e) morphology of holes and particulates, (f) morphology of accumulated particulates.

line scan results of corroded Mo. Because of the appearance of holes on the surface, the interface of platinum coating and Mo substrate shows a jagged appearance. The measured hole depth is 100–400 nm, as shown in Fig. 3(a). Fig. 3(b) shows that the EDS line scan result of Mo depletion/C enrichment depth is approximately 0.4 μm. Furthermore, the EDS elemental mapping analysis result of the corrosion section is shown in Fig. 4(a). To better understand the distribution and content of elements on the Mo surface and inside of the substrate, MATLAB was used for the superposition and to combine the mapping diagram with SEM photos; the distribution of the sum of element points in the diagram with the cross-section depth was calculated, as shown in Fig. 4(b). The results indicate that the C content on the surface of the corroded Mo substrate is considerably higher than that inside it. The C content decreases from the surface to substrate, which is consistent with the results shown in Table 2 and Fig. 3(b). These results indicate that the O, Mo, and C elements on the surface of or inside the Mo substrate are consumed in liquid Li, while the C element returns to the Mo surface due to some reactions. This will be discussed in Section 4.

3.2.2. *Microstructures of TZM samples after corrosion test*

The micrographs of the TZM surface before and after corrosion are shown in Fig. 5. The SEM image recorded at a high magnification shows a uniform and flat surface of TZM before the corrosion test. The corroded TZM sample loses its metallic lustre and exhibits nonuniform brightness after cleaning, which indicates inhomogeneous corrosion of TZM in liquid Li. After exposure to liquid Li for 500 h, as shown in Fig. 5(b) and (e), the corroded TZM surface exhibits many holes and some particulates, which is similar to the appearance of TZM samples after exposure for 1300 h. The only difference is that grain boundary corrosion is observed on the TZM surface after exposure for 1300 h, as shown in Fig. 5(d,f). From the comparison of Figs. 2 and 5, the surface micrographs of the corroded TZM and Mo show similarities and differences. The similarity is that holes appear on the surfaces of both the corroded TZM and Mo samples, as shown in Fig. 2(b,c) and (b,e). The difference is that the TZM samples suffer grain boundary corrosion and some particulates accumulate on the surface, as shown in Fig. 5(d,f). Moreover, compared to the corrosion results of 304 and 316 L SS [28], the microstructures of the corroded SS surface are similar to those of corroded TZM; however, the corroded products of the 304 SS surface and the grain boundary corrosion of 316 L SS are more severe than those of Mo and TZM.

The element distribution and content of the selected area on the corroded TZM surface were analysed using EDS. As shown in Fig. 6, after exposure to liquid Li for 500 h, the mapping diagram of the elements show enrichment of the Zr element on the TZM surface. In addition, the particulates adhered on the corroded TZM surface are rich in Ti and N. The element content of the selected area, numbered as 1–3 in Fig. 5(a,d, f), is presented in Table 3. After exposure to liquid Li for 1300 h, the

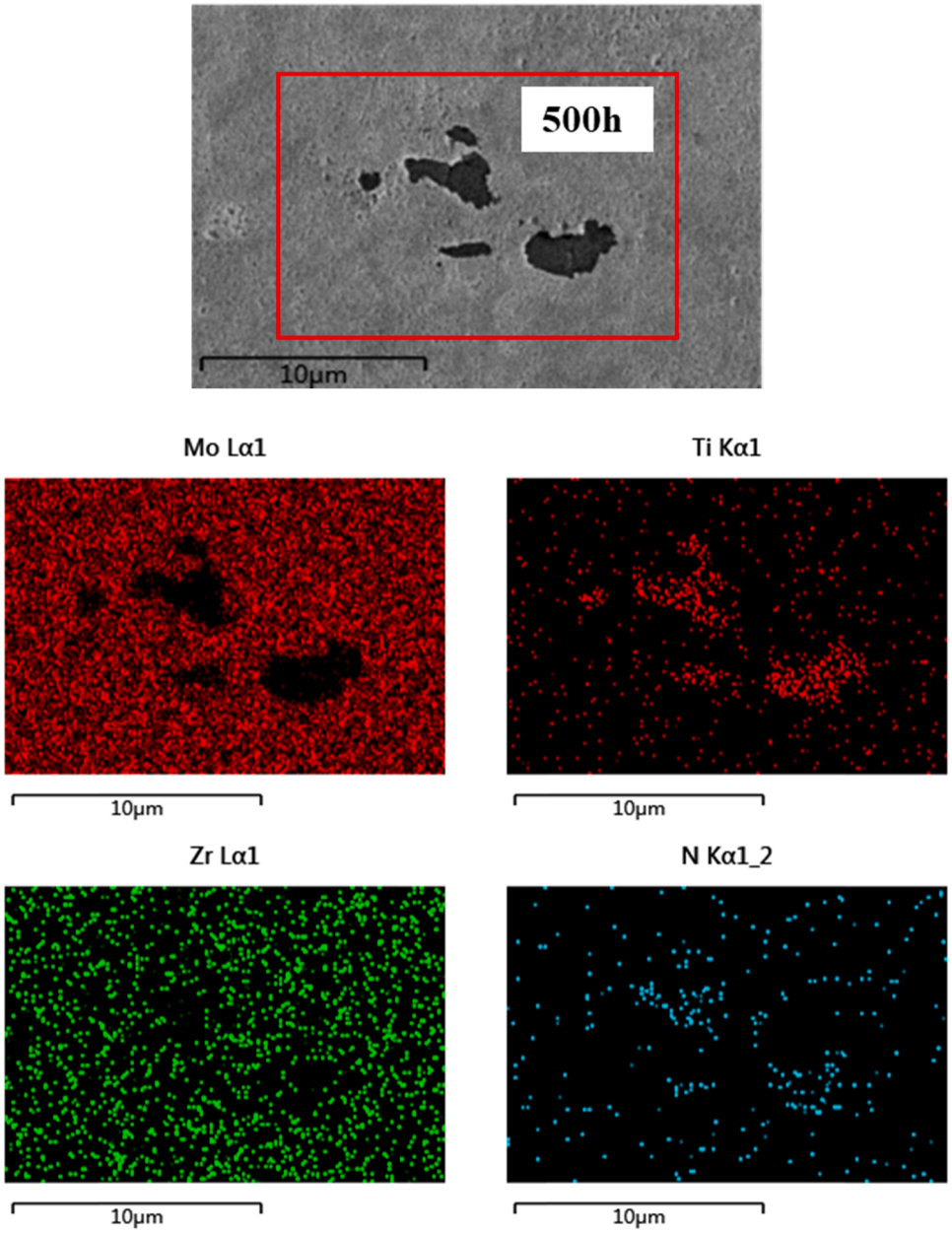

Fig. 6. Mapping of elements of the TZM sample after exposure to liquid Li for 500 h.

Table 3
Surface compositions of TZM exposed to liquid Li at 623 K for 1300 h.

Area	Surface composition (EDS result)	O	C	N	Ti	Zr	Mo
1	wt%	2.23	2.65	/	4.52	3.08	Bal
2	wt%	1.54	/	/	1.59	1.23	Bal
3	wt%	/	9.67	9.56	40.26	31.94	Bal

depletion of O, Ti, and Zr is observed on the TZM surface. However, the accumulated particulates are rich in Ti, Zr, C, and N elements. Thus, it is speculated that the particulates are a mixture of Ti/Zr carbides and nitrides. This conclusion is supported by XPS and TOF-SIMS analyses.

The cross-section of the corroded TZM sample was also cut using FIB. Fig. 7(a) and (b) show the cross-section morphology and EDS line scan analysis results of TZM after exposure to liquid Li for 1300 h. The results indicate that the corrosion depth of TZM is approximately 0.4 μm, which is consistent with the line scan result of corroded Mo, as shown in Fig. 3 (b). However, after exposure to liquid Li for 1320 h at 600 K, the corrosion depths of 304 and 316 L SS become 7.5 and 4 μm, which are considerably deeper than those of Mo and TZM [28]. In addition, Fig. 7 (b) shows that the content change of Ti and O is not evident with the cross-section depth distribution. These results indicate that the elements on the surface of TZM, such as O, C, Ti, and Zr, are consumed in liquid Li. Then, the deposition of Ti, Zr, C, and N on the TZM surface due to some reactions results in the enrichment of these elements. This will also be discussed in Section 4.

3.3. Surface composition analysis of Mo and TZM

3.3.1. XPS spectra and TOF-SIMS analysis of Mo samples

XPS and TOF-SIMS were used to analyse the surface compounds of the Mo and TZM samples before and after the corrosion test. The XPS spectra and TOF-SIMS analysis results of the Mo surface are shown in Figs. 8 and 9, respectively. As shown in the C1s spectra (Fig. 8(a)), the difference is merely that Li_2CO_3 can be found on the corroded Mo

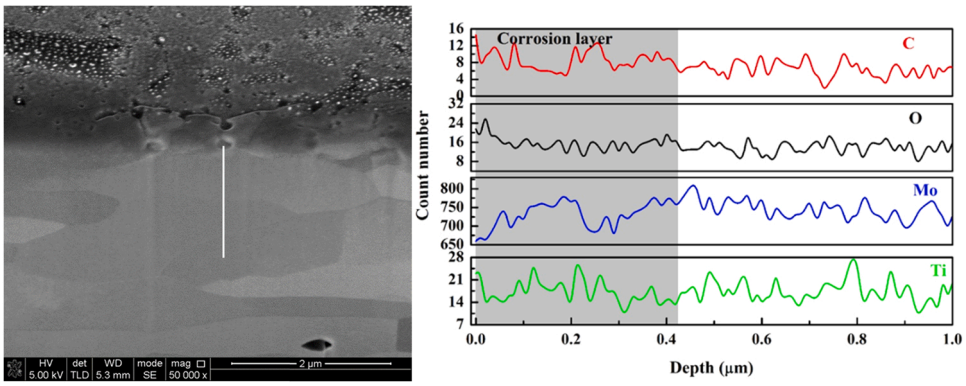

Fig. 7. Cross-section micrograph and EDS line scan results of corroded TZM after exposure to liquid Li for 1300 h.

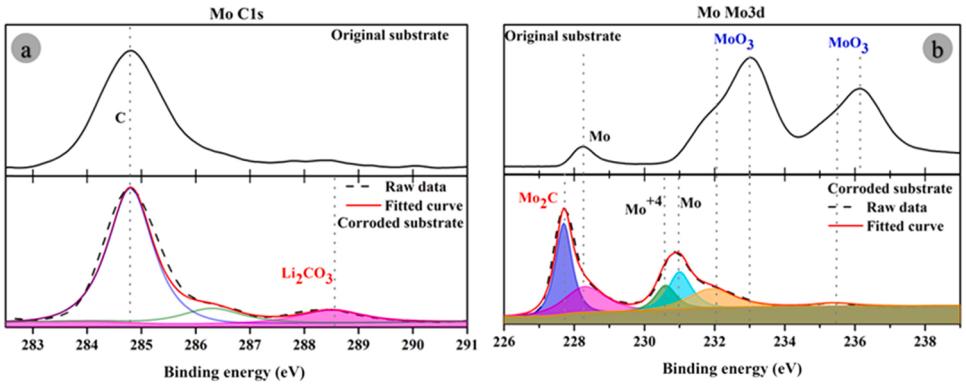

Fig. 8. XPS spectra of Mo surface before and after exposure to liquid Li for 1300 h.

surface due to the oxidation of adhered Li on the samples during transfer to the XPS system in air. Fig. 9(b,d,g) show the residues of Li, Li_2C_2, and Li_2CO_3 on the corroded surface of Mo. According to the Mo3d spectra (Fig. 8(b)), after exposure to liquid Li, MoO_3 peaks at 235.5 and 236.15 eV disappear, and the Mo peak appears at 231.0 eV along with the MoO_3 peak at 232.1 eV, which is attributed to MoO_3. This finding indicates that the reduction reactions of Mo oxide can be realised under liquid Li contact. The Mo_2C and Mo^{+4} peaks appear at 227.8 and 230.6 eV, respectively, along with the Mo peak at 228.2 and 232.1 eV, which indicates that the Mo carbonisation reactions can also be formed in high-temperature liquid Li. In addition, Mo_2C and MoC are found on the sample surface, as shown in Fig. 9(c,e). As shown in Fig. 9(g,h), Li is also found on the Mo substrate, which is attributed to the penetration of Li into the surface of corroded Mo along the holes (Fig. 2(b,c)). Moreover, the enrichment of C on the surface is detected, as shown in Fig. 9 (f). These results are consistent with the EDS surface analysis results presented in Table 2.

3.3.2. *XPS spectra and TOF-SIMS analysis of the TZM samples*

Figs. 10 and 11 show the XPS spectra and TOF-SIMS results of TZM surface before and after the corrosion test. Li_2CO_3 can also be found in the C1s spectra of the TZM sample due to the oxidation reaction of Li adhered onto the samples during transfer, as shown in Figs. 10(a) and 11 (d). The residues of Li and Li_2C_2 are detected on the surface of corroded TZM, as shown in Fig. 11(b,g). However, unlike the C1s spectra of the Mo sample (Fig. 8(a)), the TiC peak appears at 282.1 eV, which indicates that Ti carbonisation can be realised under liquid Li contact at 623 K. According to the Mo3d and Mo3p spectra (Fig. 10(b,c)), after exposure to liquid Li, the MoO_3 peaks at 236.0 and 233.0 eV disappear, and the peak intensities of MoO_3 at 235.5 and 232.1 eV decrease. In addition, the Mo peaks appear at 228.2 and 231.0 eV near the MoO_3 peak at 232.1 eV. The results indicate that the reduction of Mo oxide can be realised in liquid Li contact. This phenomenon causes O consumption on the sample surface. In addition, the Mo peak at 228.1 eV disappears after exposure to liquid Li, which indicates the consumption of the Mo element on the surface. Moreover, a Mo_2C peak appears at 227.8 eV along with the Mo peak at 228.1 eV, which is attributed to the Mo carbonisation of TZM exposed to liquid Li. Fig. 11(c,e) also show the presence of Mo_2C and MoC on the TZM surface.

The binding energy of N1s spectra is close to that of Mo3p spectra, as shown in Fig. 10(c). When exposed to liquid Li, a TiN peak appears at 397.4 eV in the N1s spectra for the corroded TZM substrate. According to Ti2p spectra (Fig. 10(d)), the Ti oxide peaks of TiO_2 and TiO observed at 459.3, 458.2, and 456.8 eV disappear after the corrosion test, and the Ti nitride peaks of $TiN_{0.24}$ and TiN appear at 454.5, 455.2, and 457.2 eV, which indicates that the reduction of Mo oxide and Ti nitriding reactions can occur in high-temperature liquid Li. In addition, TiN is observed in Fig. 11(f). Moreover, a TiC peak is found in the Ti2p spectra at 454.9 eV, which corresponds to the TiC peak at 282.1 eV in the C1s spectra. This finding proves that Ti carbonisation can be realised in liquid Li contact. The enrichment of Ti, C, and N elements on the TZM surface results from the Mo/Ti carbonisation, and Ti nitriding reactions can be realised in liquid Li. This finding is similar to the results shown in Fig. 9(g,h), where Li penetrates the substrate of the corroded TZM through the holes and grain boundary on the surface. Overall, the XPS and TOF-SIMS results obtained for the TZM surface are consistent with the EDS analysis results (Fig. 6 and Table 3).

3.4. *Surface hardness of Mo and TZM*

To study the effects of liquid Li corrosion on the mechanical properties of Mo and TZM, the Vickers hardness test was conducted on the sample surfaces before and after exposure to liquid Li, and the results were compared. Fig. 12 shows the Vickers hardness indentations of the

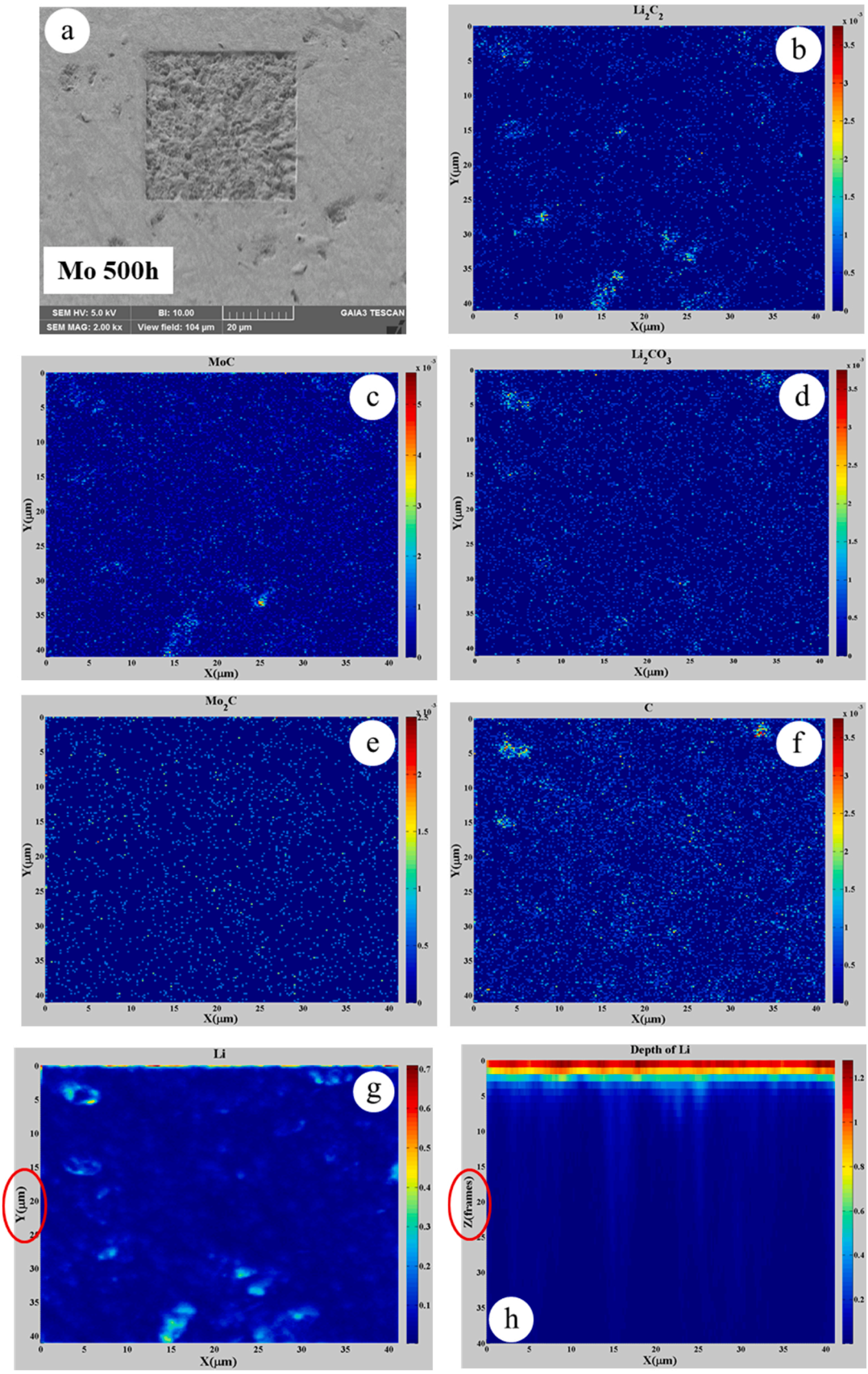

Fig. 9. TOF-SIMS results of surface compositions and distribution of corroded Mo. (a) Detection area of corroded Mo, (b) distribution of Li_2C_2, (c) distribution of MoC, (d) distribution of Li_2CO_3, (e) distribution of Mo_2C, (f) distribution of C, (g) distribution of Li, and (h) depth profile of Li intensity.

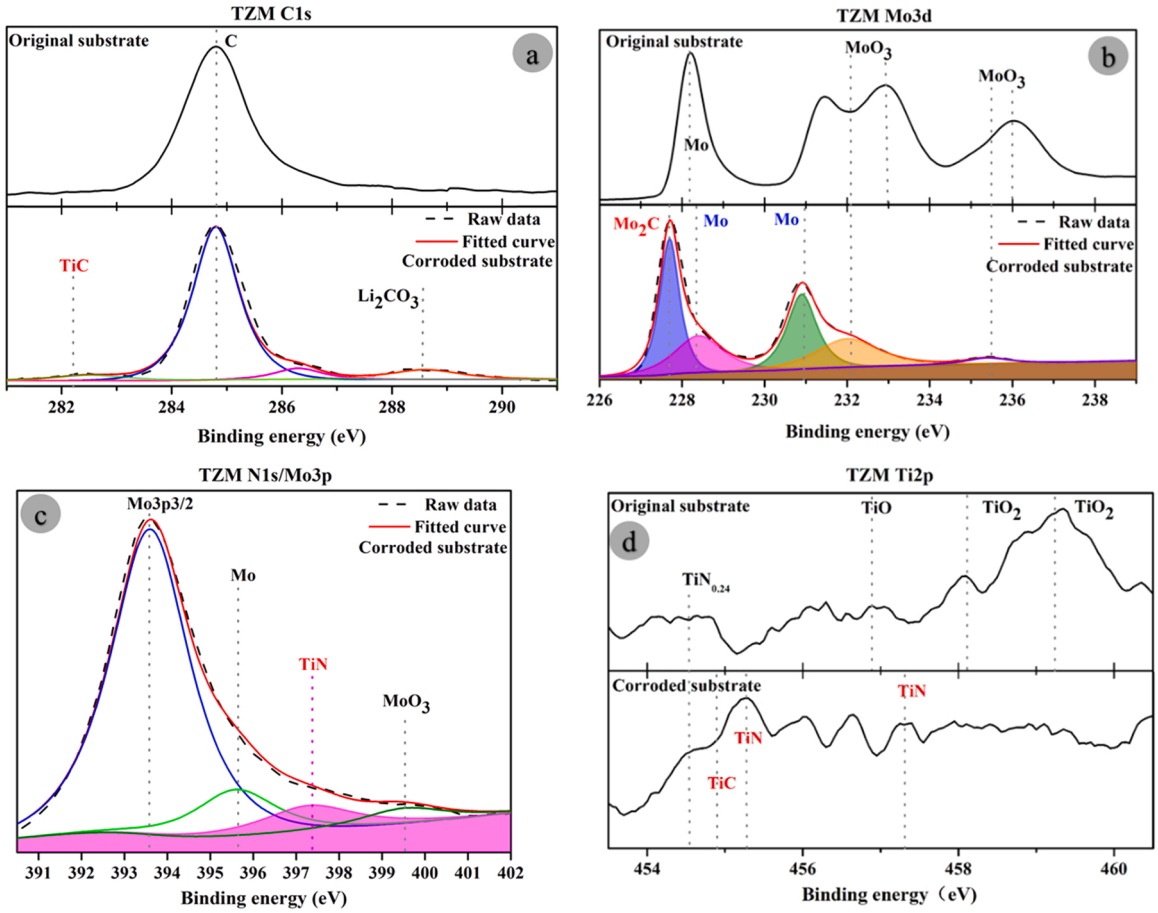

Fig. 10. XPS spectra of the TZM sample before and after the corrosion test.

Mo and TZM samples before the corrosion test. The initial average hardness of the Mo and TZM samples were 304.5 and 256.5 HV, respectively. After exposure to liquid Li at 623 K for 500 and 1300 h, the average hardness values of the corroded Mo samples were 306.1 and 305.2 HV, respectively, and those of the corroded TZM samples were 258.3 and 264.4 HV, respectively. Thus, the hardness values of Mo and TZM remain the same before and after the corrosion tests because the values of the measured points differ from each other by $< 3\%$. By contrast, after exposure to liquid Li at 600 K for 1300 h, the surface hardness values of 304 and 316 L SS increase by 10–20 HV due to the large area covered by Fe/Cr carbides [28]. This result indicates the minimal effect of liquid Li on the surface hardness of Mo and TZM.

4. Discussion

The mass loss of Mo and TZM occurs mainly because of concentration gradient driven composition transport from the solid–liquid interface of Mo/TZM and Li to liquid Li. Thus, the mass loss of the TZM samples in liquid Li can be attributed to the dissolution of elements such as Mo, Ti, and Zr. The solubility of metallic elements differs according to the temperature and type of liquid metals [29–31], that is, the selective dissolution of compositions (e.g. Mo and C or Ti and Zr elements of Mo and TZM alloys) can occur in liquid Li. At relatively low concentrations of the liquid metal solution, which occurs in a practical realised situation, the relation between temperature and the solubility of the metal or alloy components can be expressed as follows[32]:

$$\ln C = A - B/T, \quad (1)$$

where C is the impurity concentration in the liquid metal in atomic fractions (%), T is the temperature, and K, A, and B are the constants. Eq. (1) shows that the relation between solubility and temperature is expressed in a natural logarithm; thus, the solubility increases with the temperature. Fig. 13 shows the relation between temperature and the solubility of Mo, C, Zr, and Ti in high-purity Li. The saturation solubility of these elements at 623 K exhibits the following order: C > Zr > Ti > Mo. Thus, the selective dissolution of C, Zr, and Ti from TZM that occurs in liquid Li results in nonuniform corrosion. This phenomenon leads to the low availability of Zr and Ti and rich availability of Mo on the corroded TZM surface, as shown by the EDS results listed in the second row of Table 3. However, the concentration and mass of C are considerably smaller than those of other elements in TZM and Mo; thus, the contribution of C dissolution to mass loss is weaker than that of the other elements. The Mo samples show uniform corrosion under the concentration gradient driven mainly by a single composition of Mo.

In an isothermal, all-liquid system, equilibria can generally be achieved after a certain period. In theory, for solubility-driven dissolution, corrosion stops or slows down when solubility relations are satisfied. This result suggests that the highest theoretical mass loss of Mo and TZM samples is approximately 1.1×10^{-15} g for the Mo saturation concentration of 5.7×10^{-19} mol.% in liquid Li at 623 K; this loss is considerably lower than the experimental results of Mo and TZM mass losses of 1.6×10^{-4} and 3.1×10^{-4} g, respectively. This result indicates that the corrosion of Mo and TZM in liquid Li has other forms apart from the dissolution of compositions.

Additionally, according to Figs. 8–11, the corrosion of Mo and TZM in liquid Li is not only mass loss. The chemical reactions between liquid Li and compositions of Mo and TZM might occur to form the corrosion products deposited on the Mo and TZM surfaces. According to comprehensive EDS, XPS, and TOF-SIMS analyses, the chemical reactions involved include the following two forms: (1) reactions between

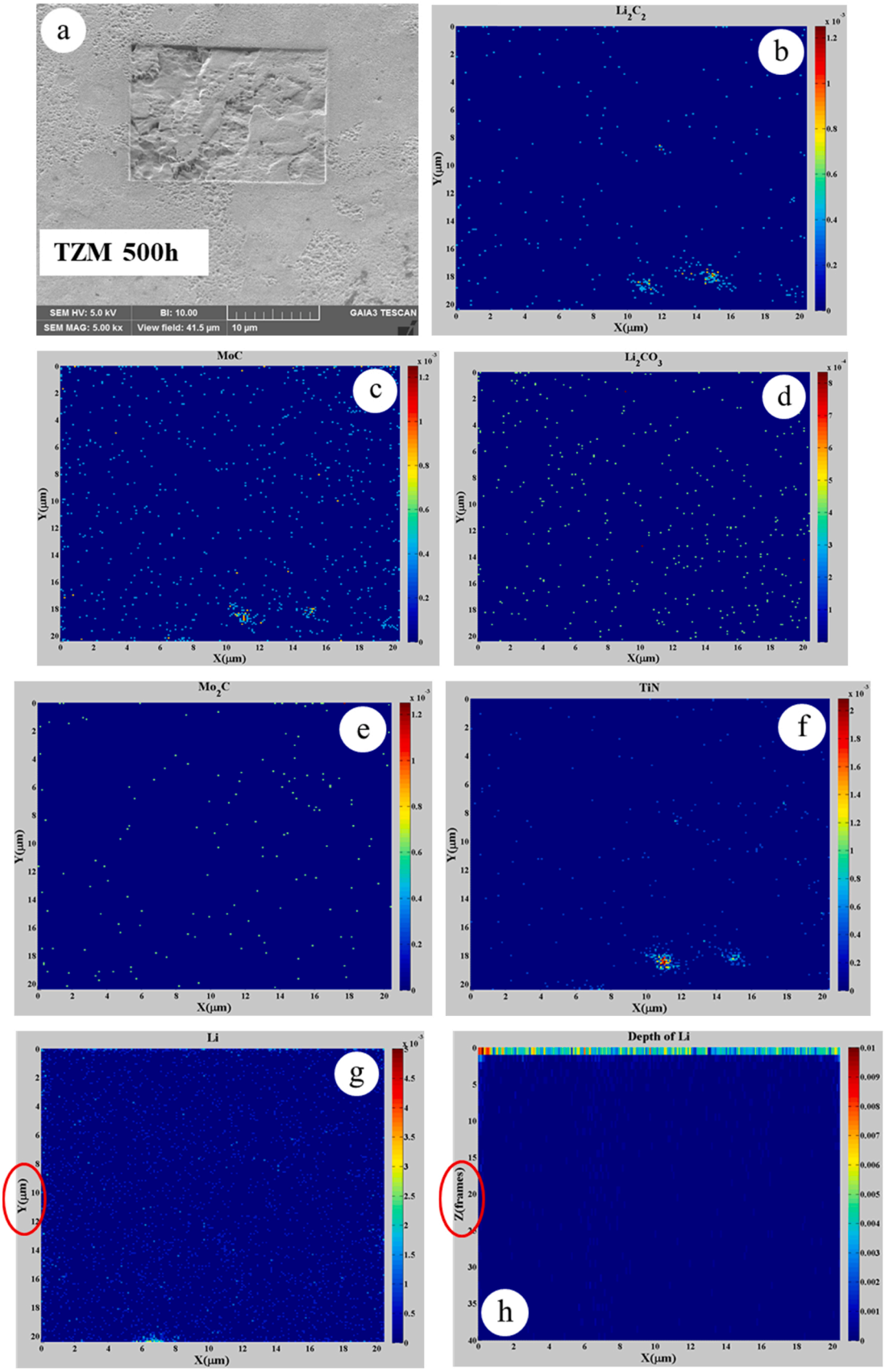

Fig. 11. TOF-SIMS results of the surface compositions and distribution of corroded TZM. (a) Detection area of corroded Mo, (b) distribution of Li_2C_2, (c) distribution of MoC, (d) distribution of Li_2CO_3, (e) distribution of Mo_2C, (f) distribution of TiN, (g) distribution of Li, and (h) depth profile of Li intensity.

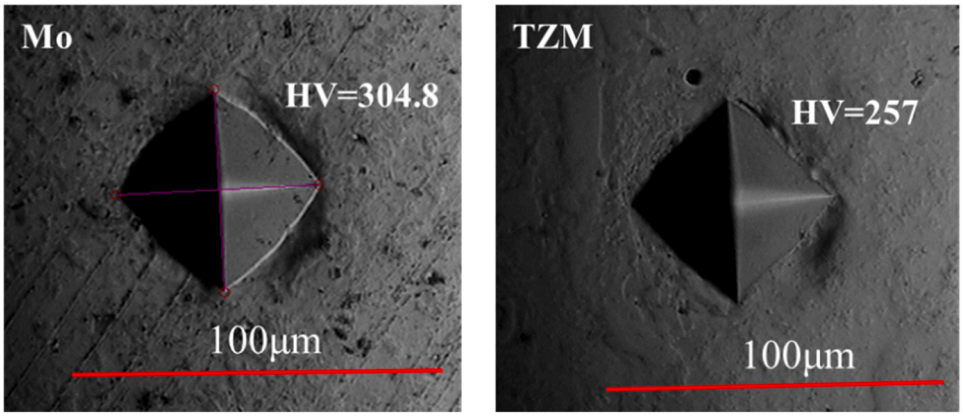

Fig. 12. Vickers hardness indentations of the Mo and TZM samples before the corrosion tests.

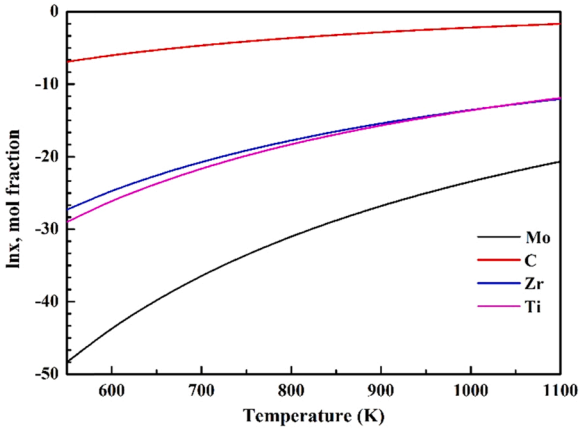

Fig. 13. Solubility of elements in high-purity liquid Li with temperature.

liquid Li and the surface compositions of Mo/TZM in the liquid–solid interface and (2) reactions between the dissolved elements from the samples and liquid Li. In the first part, the following reactions occur at the solid–liquid interface when liquid Li comes in contact with Mo and TZM:

$$MoO_3(s)+6Li(l)=3Li_2O(s)+Mo(s)\ (623K,\Delta G=-971.4kJ) \quad (2)$$

$$TiO_2(s)+4Li(l)=2Li_2O(s)+Ti(s)\ (623K,\ \Delta G=-208{\cdot}1kJ) \quad (3)$$

Eqs. (2) and (3) indicate that the reduction reactions of Mo and Ti oxides can be realised in liquid Li contact, which corresponds to the results shown in Fig. 8(b) and 10(b). In addition, these reactions are the main reasons for O depletion from the sample surface, which agrees with the results shown in Tables 2 and 3. The Mo and TZM substrates are exposed to liquid Li and the compositions of Mo and TZM dissolved in liquid Li when the oxide protective layer is depleted by liquid Li.

As confirmed by Refs. [31,33] and Fig. 13, C is preferably dissolves in liquid Li and forms Li_2C_2, as shown in Fig. 9(b) and 11(b). In the second part, the following reaction occurs:

$$2C(s)+2Li(l)=Li_2C_2(s)\ (623K,\ \Delta G=-51{\cdot}3kJ) \quad (4)$$

This reaction is the reason behind C depletion from Mo and TZM into liquid Li. Refs. [29,34] have shown that holes appear near the SS surface because C from the SS substructure dissolves in liquid Li. Therefore, despite the weak contribution of C dissolution to the mass loss, C plays an important role in chemical corrosion, which results in pitting, as shown in Figs. 2 and 5. Additionally, as reported by Xu et al. [30], Mo acts as a C-trapper, and the C potential in liquid Li can be controlled by forming Mo carbides on the inner surface of the Mo crucible. Hence, during the corrosion tests, the following reactions can occur:

$$2Mo(s)+C(s)\xrightarrow{\Delta}Mo_2C(s)(623K,\ \Delta G=-55.5kJ), \quad (5)$$

$$4Mo(s)+3Li_2C_2(s)\xrightarrow{\Delta}2Mo_2C(s)+6Li\ (l)(623\ K,\ \Delta G=-201.5\ kJ). \quad (6)$$

Free C in the Mo substrate can be captured by Mo to form a stable Mo carbide, which is fixed in the substrate. Moreover, the C atoms and Li_2C_2 compound dissolved in liquid Li are captured by Mo to form Mo_2C and then are deposited on the Mo and TZM surfaces through movement, as shown by the XPS and TOF-SIMS results (Fig. 8(b), 9(c,e), 10(b), and 11 (c,e)). Reactions (5,6) also correspond to the results shown in Tables 2 and 3 for the enrichment of the C element on the surface of the Mo and TZM samples. For the TZM corrosion results, as shown in Fig. 10(a,c,d), the TiC and TiN compounds are detected on the corroded surface. Table 3 shows that the content of Zr and Ti elements on the corroded surface is higher than that on the original surface. These phenomena can be explained by the following chemical reactions:

$$2Ti(s)+Li_2C_2(s)\xrightarrow{\Delta}2TiC(s)+2Li(l)(623\ K,\Delta G=-295.7\ kJ), \quad (7)$$

$$2Zr(s)+Li_2C_2(s)\xrightarrow{\Delta}2ZrC(s)+2Li(l)(623\ K,\Delta G=-329.4\ kJ) \quad (8)$$

Furthermore, as confirmed by ref. [29], the solubility of N is higher than that of other nonmetallic elements of C, O, and H in liquid Li. As shown in Table 1, the N content in liquid Li and TZM is 0.002–0.003 wt %. It is easy for the dissolved N reacting with liquid Li to form Li nitride. For the TZM corrosion test, the possible chemical reactions of nitrides in liquid Li are as follows:

$$6Li(l)+N_2(g)\rightarrow 2Li_3N(s)\ (623\ K,\ \Delta G=-169{\cdot}6\ kJ), \quad (9)$$

$$Li_3N(s)+Ti(s)\xrightarrow{\Delta}3Li(l)+TiN(s)(623\ K,\Delta G=-193.1\ kJ), \quad (10)$$

$$Li_3N(s)+Zr(s)\xrightarrow{\Delta}3Li(l)+ZrN(s)(623\ K,\Delta G=-221.3\ kJ). \quad (11)$$

The standard Gibbs free energy of reactions (9−11) is negative, which indicates that Ti and Zr are N trapped in liquid Li. The Zr and Ti nitrides transfer and adhere to the TZM surface when the corrosion products of nitrides are formed, which results in the enrichment of Ti, Zr, and N elements on the surface of TZM samples, as shown in Figs. 6, 10(c, d) and 11(f).

In addition, to better understand the corrosion kinetics of Mo and TZM in liquid Li, the migration and reaction mechanisms of the elements dissolved in liquid Li were studied at the atomistic scale by using the Ab-initio molecular dynamics (AIMD) simulation. All AIMD simulations were performed at 700 K. The dimensions of the simulation domain were $15 \times 15 \times 15$ Å^3, including 75 atoms (70 Li atoms, 1 metallic solute atom, and 4 impurity atoms). Fig. 14 shows the initial structure of

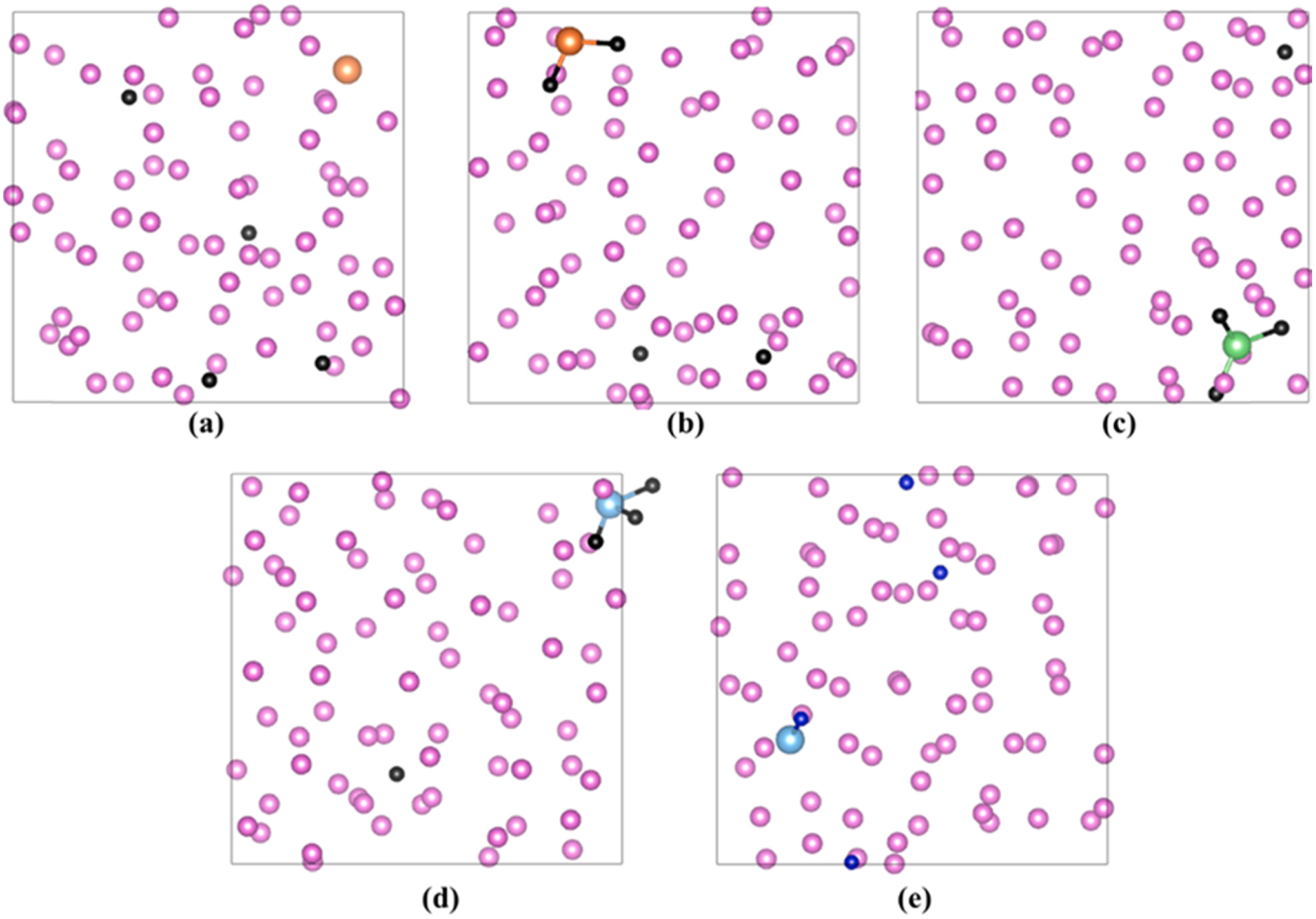

Fig. 14. AIMD simulation results. (a) Initial structure of one Zr atom and four C atoms dispersed in liquid Li. (b)–(d) Structures of solute atoms and C atoms after 120 ps simulation. (e) Structure of one Ti atom and four N atoms after 120 ps simulation. Purple, orange, green, cyan, black, and blue spheres represent Li, Mo, Zr, Ti, C, and N atoms, respectively. (For interpretation of the references to colour in this figure legend, the reader is referred to the web version of this article.)

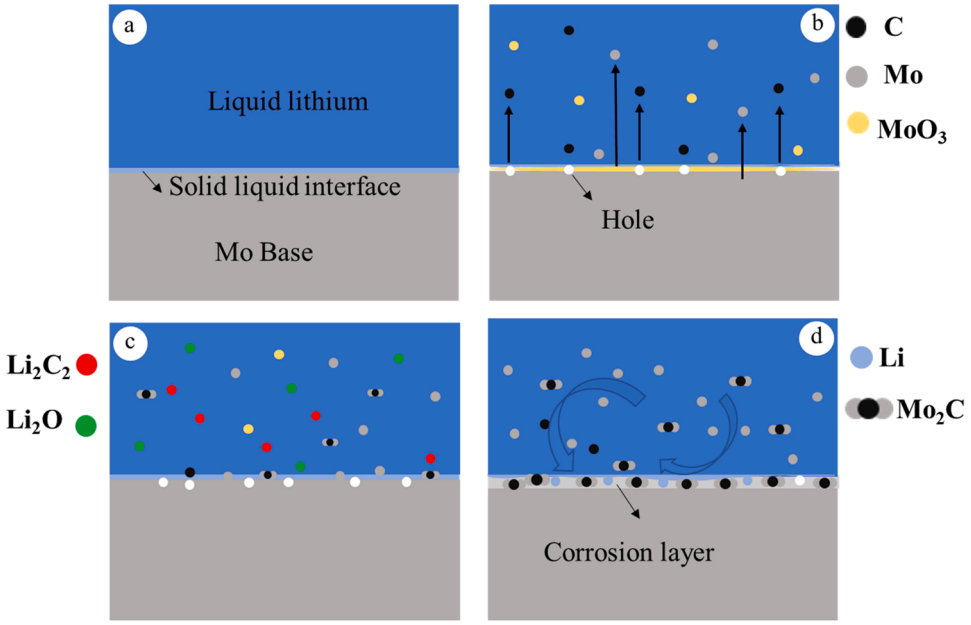

Fig. 15. Corrosion process of Mo in liquid Li. (a) Initial state of Li contacts with Mo, (b) liquid Li destroys the oxide layer of Mo surface, (c) compositions from the Mo dissolve into liquid Li and react with Li, and (d) corrosion products are deposited on the Mo surface.

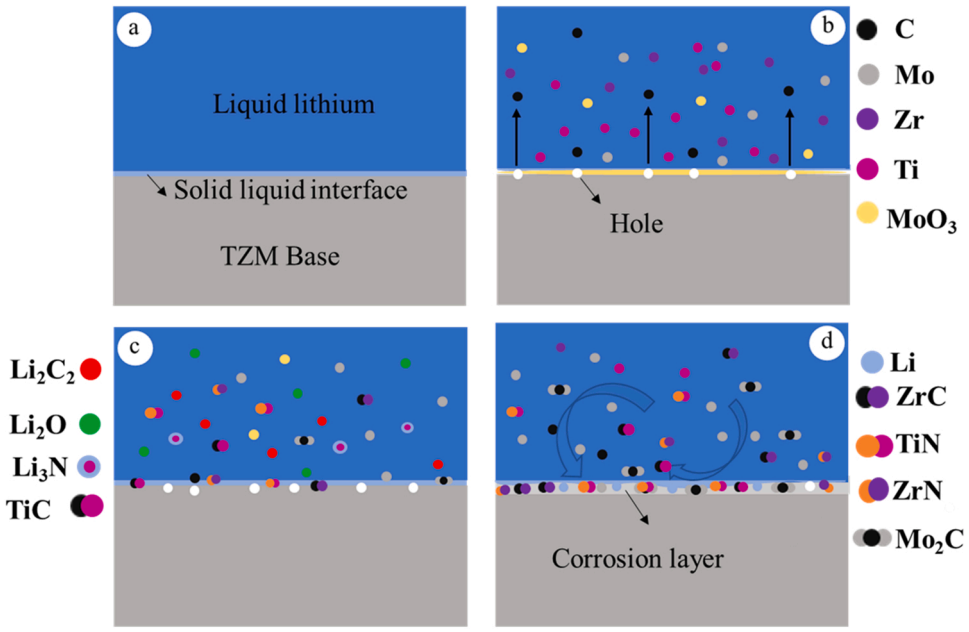

Fig. 16. Corrosion of TZM in liquid Li. (a) Initial state of Li contact with TZM, (b) liquid Li destroys the oxide layer, (c) compositions dissolve into liquid Li and react with Li, and (d) corrosion products are deposited on the TZM surface.

the liquid system, in which the metallic solute atom is far away from the C atoms. After 120-ps simulation, the solute atoms (Mo, Zr, or Ti) can bind with the C atoms to form small carbide molecules. In addition, Ti and N atoms can aggregate to form a TiN dimer after 120 ps. These AIMD simulation results are in a strong agreement with the XPS and TOF-SIMS results and confirm the carbonisation and nitridation reactions presented in Eqs. (4–11).

Overall, the results indicate that physical dissolution and chemical reactions are two main processes involved in the corrosion of Mo and TZM conducted in liquid Li. These two processes promote and complement each other. By contrast, the chemical reactions play a key role in the corrosion of Mo, especially in that of TZM alloy. Therefore, in liquid Li, the corrosion mechanism of Mo and TZM is the same, while the corrosion process is slightly different.

The corrosion of Mo in liquid Li is shown in Fig. 15. First, the reduction of MoO_3 (Eq. 2) occurs on the Mo–Li solid–liquid interface when the Mo comes in contact liquid Li; simultaneously, free C and Mo on the surface begin to dissolve into liquid Li, which results in pitting and mass loss. Dissolved free C is first captured by Li to form Li_2C_2 (Eq. 4) and then is dissociated by Mo to form a highly stable carbide of Mo_2C (Eq. 6). Free C on the inner surface of the Mo substrate can also be captured by Mo atoms to form Mo_2C (Eq. 5) and be fixed on the substrate during corrosion. The corrosion product of Mo_2C formed in liquid Li is deposited on the Mo sample surface through the diffusion movement, which leads to the enrichment of C element on the surface of the Mo material. In addition, liquid Li can easily permeate the inner surface of the Mo substrate through the surface holes, which intensifies the corrosion of Mo and leads to the appearance of a certain depth of corrosion layer. However, the Vickers hardness of the surface remains almost unaffected due to the shallow depth of the corrosion layer.

Fig. 16 shows the corrosion of TZM, which is slightly different from that of Mo, in liquid Li. When liquid Li comes in contact with the TZM alloy, the reduction of MoO_3 (Eq. 2) and TiO_2 (Eq. 3) occurs at the solid–liquid interface, and free C, Ti, Zr, and Mo avail be on the TZM surface begin to dissolve into liquid Li. Due to the difference in the solubilities of these elements in liquid Li, selective dissolution of free C, Ti, and Zr elements occurs, which eventually leads to pitting and grain boundary corrosion on the TZM surface. Similar to the corrosion of Mo, free C dissolved in liquid Li is first captured by Li to form Li_2C_2 (Eq. 4) and then is snatched by Zr, Ti, and Mo to form highly stable carbides of ZrC, TiC, and Mo_2C, respectively (Eqs. 6–8). In addition, free N available in Li and on the TZM surface is captured by liquid Li to form Li_3N (Eq. 9) and then is captured by Zr and Ti to form ZrN (Eq. 11) and TiN (Eq. 10), respectively. The carbides and nitrides adhere to the TZM surface when the reactions occur near the solid–liquid interface, and the corrosion products formed in liquid Li travel to the TZM alloy surface, which results in the enrichment of C, N, Ti, and Zr elements. In addition, the TZM alloy loses its metallic lustre due to the deposition of carbides and nitrides and shows an inhomogeneous brightness. TZM corrosion also intensifies because liquid Li penetrates the interior of the TZM substrate from the holes and grain boundary on the surface, which results in increased mass loss, surface damage, and a deep corrosion layer. Similarly, during the corrosion test, the free C element in the interior of the TZM substrate can be captured to form stable carbides and fixed.

According to these results, corrosion in liquid Li does not appear to be a serious problem for Mo at 623 K during 1300 h. However, corrosion can be problematic for TZM under a long-term exposure to liquid Li. In these cases, a possible influence of Li might be the depletion of C, Zr, and Ti elements and resulting pitting and grain boundary corrosion. By comparing the compositions and contents of TZM and Mo, the compositions of 0.5 wt% Ti and 0.09 wt% Zr were added to TZM. Thus, the mechanical properties of TZM alloy significantly improved compared with that of Mo. This discussion indicates that the high contents of C, Ti, Zr, and N elements in TZM increase not only the amount of dissolution in liquid Li but also the corrosion products of carbides and nitrides on the TZM surface. This phenomenon results in comparatively higher mass loss, more corrosion products, and a deeper corrosion layer. Therefore, reducing the contents of nonmetallic elements of N and C in TZM and liquid Li can effectively alleviate TZM corrosion. Eqs. (6–8) indicate that the carbide products of Mo_2C, TiC, and ZrC are highly stable in liquid Li. Hence, increasing the amount of stable carbides on the surface of and inside Mo-based materials during production and preparation helps in improving the corrosion resistance in liquid Li. For example, high-temperature prolonged baking is a simple approach to increase the amount of carbides in Mo-based materials. Even under the assumption of meeting the requirements of the material properties, Ti and Zr elements in the Mo alloy can be replaced with other elements (e.g. Ta and W), which are less soluble in liquid Li than Mo to alleviate corrosion

resulting from the dissolution of preferred elements. In the future, we will verify the aforementioned conclusion through several corrosion experiments.

5. Conclusions

The corrosion behaviours of Mo and the TZM alloy in liquid Li at 623 K in the Ar atmosphere were investigated and compared. The following main conclusions are drawn:

(1) Corrosion in liquid Li does not appear to be a serious problem for Mo at 623 K. However, corrosion can be problematic for TZM under long-term exposure to liquid Li.
(2) After corrosion, the Mo samples demonstrate homogeneous corrosion except pitting, and the TZM samples show nonuniform corrosion with pitting and grain boundary corrosion.
(3) After exposure to liquid Li for 1300 h, the weight loss rates of Mo and TZM become 4.0×10^{-4} and 7.8×10^{-4} $g{\cdot}m^{-2}{\cdot}h^{-1}$, respectively, which are equivalent to 0.34 and 0.67 $mm{\cdot}a^{-1}$ average corrosion depth rates, respectively.
(4) The corrosion of TZM is more severe than that of Mo in liquid Li because of the addition of Ti (0.5 wt%) and Zr (0.09 wt%) to TZM. The selective dissolution of C, Ti, and Zr elements and chemical reaction of carbides and nitrides enhance TZM corrosion.
(5) Reducing the nonmetallic contents of N and C in TZM and liquid Li can effectively alleviate TZM corrosion. In addition, increasing the amount of stable carbides on the surface of and inside Mo-based materials can help improve the corrosion resistance in liquid Li.

CRediT authorship contribution statement

X.C. Meng: Conceptualization, Investigation, Methodology, Writing – original draft. **L. Li:** Data curation, Investigation, Visualization. **C.L. Li:** Investigation, Visualization, Methodology. **D. Andruczyk:** Investigation, Methodology. **K. Tritz:** Writing – review & editing. **R. Maingi:** Writing – review & editing. **H. Ming:** Investigation, Data Curation. **D.H. Zhang:** Investigation, Writing – original draft. **W. Xu:** Software, Investigation. **Z. Sun**: Data curation, Formal analysis. **G.Z. Zuo:** Project administration, Writing – review & editing. **J. S. Hu:** Project administration, Validation, Supervision.

Declaration of Competing Interest

The authors declare that they have no known competing financial interests or personal relationships that could have appeared to influence the work reported in this paper.

Acknowledgments

The authors would like to acknowledge Dr. Z. X. Liu in Hunan University for AIMD simulations and fruitful discussion. And this research is funded by National Nature Science Foundation of China under the contract Nos. 119050138, 11625524, 11775261, 11905148, 12105135. National Key Research and Development Program of China (2017YFA04025000 and 2017YFE030110). Users with Excellence Program of Hefei Science Center CAS (2020HSC-UE010). The Institute of Energy, Hefei Comprehensive National Science Center under Grant Nos. 21KZS202 and 21KZS208. Interdisciplinary and Collaborative Teams of CAS.

References

[1] T. Flament, P. Tortorelli, V. Coen, H.U. Borgstedt, Compatibility of materials in fusion first wall and blanket structures cooled by liquid metals, J. Nucl. Mater. 191–194 (1992) 132–138.
[2] T. Terai, T. Yoneoka, H. Tanaka, A. Suzuki, S. Tanaka, M. Nakamichi, H. Kawamura, K. Miyajima, Y. Harada, Compatibility of yttria (Y_2O_3) with liquid lithium, J. Nucl. Mater. 233–237 (1996) 1421–1426.
[3] S. Malang, Development of insulating coatings for liquid metal blankets, Fusion Eng. Des. 27 (1995) 570–586.
[4] X.L. Xu, Q.J. Fu, Nuclear fusion reactor materials and corrosion, J. Mater. Sci. Eng. 10 (1992) 17–20.
[5] J.S. Hu, Z. Sun, H.Y. Guo, J.G. Li, B.N. Wan, H.Q. Wang, S.Y. Ding, G.S. Xu, Y. F. Liang, D.K. Mansfield, R. Maingi, X.L. Zou, L. Wang, J. Ren, G.Z. Zuo, L. Zhang, Y.M. Duan, T.H. Shi, L.Q. Hu, t East, New steady-state quiescent high-confinement plasma in an experimental advanced superconducting tokamak, Phys. Rev. Lett. 114 (2015), 055001.
[6] T. Loarer, S. Brezinsek, V. Philipps, J. Bucalossi, D. Douai, H.G. Esser, S. Grunhagen, J. Hobirk, S. Jachmich, E. Joffrin, U. Kruezi, C. Lowry, G. Matthews, R. Smith, E. Tsitrone, S. Vartanian, Comparison of long term fuel retention in JET between carbon and the ITER-Like Wall, J. Nucl. Mater. 438 (2013) S108–S113.
[7] J. Li, H.Y. Guo, B.N. Wan, X.Z. Gong, Y.F. Liang, G.S. Xu, K.F. Gan, J.S. Hu, H. Q. Wang, L. Wang, L. Zeng, Y.P. Zhao, P. Denner, G.L. Jackson, A. Loarte, R. Maingi, J.E. Menard, M. Rack, X.L. Zou, A long-pulse high-confinement plasma regime in the experimental advanced superconducting tokamak, Nat. Phys. 9 (2013) 817–821.
[8] G.Z. Zuo, J.S. Hu, S. Zhen, J.G. Li, D.K. Mansfield, B. Cao, J.H. Wu, L.E. Zakharov, Comparison of various wall conditionings on the reduction of H content and particle recycling in EAST, Plasma Phys. Control. Fusion 54 (2012), 015014.
[9] M.A. Jaworski, T. Abrams, J.P. Allain, M.G. Bell, R.E. Bell, A. Diallo, T.K. Gray, S. P. Gerhardt, R. Kaita, H.W. Kugel, B.P. LeBlanc, R. Maingi, A.G. McLean, J. Menard, R. Nygren, M. Ono, M. Podesta, A.L. Roquemore, S.A. Sabbagh, F. Scotti, C.H. Skinner, V.A. Soukhanovskii, D.P. Stotler, Liquid lithium divertor characteristics and plasma–material interactions in NSTX high-performance plasmas, Nucl. Fusion 53 (2013), 083032.
[10] S.V. Mirnov, E.A. Azizov, V.A. Evtikhin, V.B. Lazarev, I.E. Lyublinski, A.V. Vertkov, D.Y. Prokhorov, Experiments with lithium limiter on T-11M tokamak and applications of the lithium capillary-pore system in future fusion reactor devices, Plasma Phys. Control. Fusion 48 (2006) 821–837.
[11] R. Majeski, S. Jardin, R. Kaita, T. Gray, P. Marfuta, J. Spaleta, J. Timberlake, L. Zakharov, G. Antar, R. Doerner, S. Luckhardt, R. Seraydarian, V. Soukhanovskii, R. Maingi, M. Finkenthal, D. Stutman, D. Rodgers, S. Angelini, Recent liquid lithium limiter experiments in CDX-U, Nucl. Fusion 45 (2005) 519–523.
[12] J.S. Hu, G.Z. Zuo, J. Ren, Q.X. Yang, Z.X. Chen, H. Xu, L.E. Zakharov, R. Maingi, C. Gentile, X.C. Meng, Z. Sun, W. Xu, Y. Chen, D. Fan, N. Yan, Y.M. Duan, Z. D. Yang, H.L. Zhao, Y.T. Song, X.D. Zhang, B.N. Wan, J.G. Li, First results of the use of a continuously flowing lithium limiter in high performance discharges in the EAST device, Nucl. Fusion 56 (2016), 046011.
[13] G.Z. Zuo, J.S. Hu, J.G. Li, N.C. Luo, L.E. Zakharov, L. Zhang, A. Ti, First results of lithium experiments on EAST and HT-7, J. Nucl. Mater. 415 (2011) S1062–S1066.
[14] G. Mazzitelli, M.L. Apicella, V.P. Ridolfini, G. Apruzzese, R. De Angelis, D. Frigione, E. Giovannozzi, L. Gabellieri, G. Granucci, C. Mazzotta, M. Marinucci, A. Romano, O. Tudisco, A. Alekseyev, I. Ljublinski, A. Vertkov, Review of FTU results with the liquid lithium limiter, Fusion Eng. Des. 85 (2010) 896–901.
[15] J. Saito, M. Morinaga, S. Kano, M. Furui, K. Noda, Corrosion behavior of Mo-Re based alloy in liquid Li, J. Nucl. Mater. 264 (1999) 206–215.
[16] J. Saito, S. Inoue, S. Kano, T. Yuzawa, M. Furui, M. Morinaga, Alloying effects on the corrosion behavior of binary Nb-based and Mo-based alloys in liquid Li, J. Nucl. Mater. 264 (1999) 216–277.
[17] R.A. Langley, P. Lamarche, Vacuum pumping requirement considerations for future fusion devices, J. Nucl. Mater. 200 (1993) 326–331.
[18] P. Fiflis, A. Press, W. Xu, D. Andruczyk, D. Curreli, D.N. Ruzic, Wetting properties of liquid lithium on select fusion relevant surfaces, Fusion Eng. Des. 89 (2014) 2827–2832.
[19] G.Z. Zuo, J.S. Hu, J. Ren, Z. Sun, Q.X. Yang, J.G. Li, L.E. Zakharov, D.K. Mansfield, Methods and preliminary measurement results of liquid Li wettability, Rev. Sci. Instrum. 85 (2014), 023506.
[20] M.L. Apicella, G. Mazzitelli, V. Pericoli Ridolfini, V. Lazarev, A. Alekseyev, A. Vertkov, R. Zagórski, First experiments with lithium limiter on FTU, J. Nucl. Mater. 363–365 (2007) 1346–1351.
[21] S. Inoue, J. Saito, S. Kano, et al. Symp. on Advanced Materials and Technology for the 21th Century[C]// Symp. on Advanced Materials and Technology for the 21th Century. Honolulu,The Japan Institute of Metals. p. 194.
[22] H. Katsuta, K. Furukawa, Air contamination effects on the compatibility of liquid lithium with molybdenum; TZM, niobium, stainless steels, nickel and hastelloy N in stainless-steel vessels at 600°C, J. Nucl. Mater. 71 (1977) 95–104.
[23] P. He, Z. Zhang, W. Xia, L. Shu, X. Ma, F. Gou, K. Zhang, Compatibility between high-flux helium plasma irradiated molybdenum and liquid lithium, J. Nucl. Mater. 509 (2018) 736–741.

[24] G.Z. Zuo, C.L. Li, R. Maingi, X.C. Meng, Z. Sun, W. Xu, Y.Z. Qian, M. Huang, Z. L. Tang, D.H. Zhang, L. Zhang, Y.J. Chen, S.T. Mao, Y.M. Wang, H.L. Zhao, D. Andruczyk, K. Tritz, X.Z. Gong, J.S. Hu, Results from a new flowing liquid Li limiter with TZM substrate during high confinement plasmas in the EAST device, Phys. Plasmas 27 (2020), 052506.
[25] S. Malang, A.R. Raffray, A. Sagara, A. Ying, Range of blanket concepts from near term solutions to advanced concepts, Fus. Eng. Des. 61–62 (2002) 295–306.
[26] Dai-Kai Sze, Michael C. Billone, Thanh Q. Hua, The ARIES-RS power core—recent development in Li/V designs, Fus. Eng. Des. 41 (1998) 371–376.
[27] X. Meng, G. Zuo, J. Ren, W. Xu, Z. Sun, M. Huang, W. Hu, J. Hu, H. Deng, Study of the corrosion behaviors of 304 austenite stainless steel specimens exposed to static liquid lithium at 600 K, J. Nucl. Mater. 480 (2016) 25–31.
[28] D.H. Zhang, X.C. Meng, G.Z. Zuo, M. Huang, L. Li, W. Xu, C.L. Li, Z.L. Tang, J. S. Yuan, Y.B. Liu, X.G. Cao, J.S. Hu, Study of the corrosion characteristics of 304 and 316L stainless steel in the static liquid lithium, J. Nucl. Mater. 553 (2021), 153032.
[29] Y. Li, H. Abe, T. Nagasaka, T. Muroga, M. Kondo, Corrosion behavior of 9Cr-ODS steel in stagnant liquid lithium and lead–lithium at 873K, J. Nucl. Mater. 443 (2013) 200–206.
[30] I.E. Lyublinski, V.A. Evtikhin, V.Y. Pankratov, V.P. Krasin, Numerical and experimental determination of metallic solubilities in liquid lithium, lithium-containing nonmetallic impurities, lead and lead-lithium eutectic, J. Nucl. Mater. 224 (1995) 288–292.
[31] K. Natesan, Influence of nonmetallic elements on the compatibility of structural materials with liquid alkali metals, J. Nucl. Mater. 115 (1983) 251–262.
[32] I.E. Lyublinski, A.V. Vertkov, V.A. Evtikhin, Application of lithium in systems of fusion reactors. 1 Physical and chemical properties of lithium, Plasma Devices Oper. 17 (2009) 42–72.
[33] R.J. Pulham, P. Hubberstey, Comparison of chemical reactions in liquid lithium with those in liquid sodium, J. Nucl. Mater. 115 (1983) 239–250.
[34] Q. Xu, M. Kondo, T. Nagasaka, T. Muroga, O. Yeliseyeva, Effect of chemical potential of carbon on phase transformation and corrosion of JLF-1 steel in a static lithium, J. Nucl. Mater. 394 (2009) 20–25.